Longitudinal Multifoci Metalens for Circularly Polarized Light

Xianzhong Chen, Ming Chen, Muhammad Qasim Mehmood, Dandan Wen, Fuyong Yue, Cheng-Wei Qiu,* and Shuang Zhang**

Metamaterials with artificially engineered subwavelength structures have been used to control the propagation of electromagnetic waves, as well as other forms of waves, such as acoustic,[1,2] elastic,[3,4] mechanical,[5–7] and matter waves,[8] to an unprecedented level, leading to highly unconventional and versatile functionalities compared with their natural counterparts.[1–12] Examples include negative refraction,[13,14] super imaging,[15,16] invisibility cloaking,[17–21] and so on. Recently, metasurfaces, a 2D counterpart to metamaterials, have attracted much attention due to their distinguished features and simplicity of fabrication. Metasurfaces consist of a monolayer of artificial atoms and are capable of manipulating light in a desirable manner by imparting local and space-variant abrupt phase change[22–24] on an incident electromagnetic wave, breaking our dependence on phase accumulation due to the propagation effect. At the interface of a metasurface, wave front shaping is accomplished within a distance much smaller than the wavelength of light beam, thus providing new opportunity to develop ultrathin devices that are easy to integrate into compact platforms. On the other hand, to circumvent the limitation of bulky optical components in conventional integrated optics, ultrathin optical devices are desirable for device miniaturization. By carefully designing subwavelength structures, metasurfaces can enable us to engineer the spatial distribution of amplitude, phase, and polarization response in subwavelength resolution, which have been used to develop a plethora of ultrathin devices, such as wave plates for generating vortex beams,[25,26] ultrathin metalenses,[27,28] aberration-free quarter-wave plates (QWPs),[29] spin-hall effect of light and spin-controlled photonics,[30,31] unidirectional surface plasmon polariton excitation[31–34] and 3D optical holography.[35–38]

As a fundamental optical device, a lens lies in the heart of many important applications in various scientific communities such as physics, optics, biology, medicine, and security. People have been fascinated by using different technologies to develop lenses with unusual features, such as ultrathin metalenses based on metasurface[27,28,39,40] and multifoci diffractive lenses[41,42] based on diffraction optics. A multifoci diffractive lens allows a single incident beam to focus at different positions along the longitudinal axis or along the transverse direction, which has been widely used in imaging systems, detectors, optical data storage, laser printing and optical free-space communications.[41–44] However, all the polarization states of the focal points are the same as that of the incident light. Moreover, the traditional method to design and fabricate such a lens is based on diffractive optics, thus the thickness is much larger than the wavelength of light. While there has been great progress in the miniaturization of optical lenses by using metasurfaces, much attention has been paid to constructing a lens with a single focal point by using different geometry structures such as V-shape,[22,23,45,46] nanorods,[27,32,36] and nanoslits.[47] Although the work on metasurface lenses is in its infancy, it offers in the long run major opportunities if multifunction nanostructured lenses can be experimentally realized in ultrathin and flat configurations. Here, we apply the concept of controllable interfacial phase discontinuity to realize an ultrathin flat metasurface lens with multiple focal points along the longitudinal direction. Unlike the traditional multifoci diffractive lenses, the position and the polarization of the focal points can be controlled by changing the helicity of the incident light. Furthermore, the developed devices are ultrathin (40 nm) and planar, which can facilitate the system integration.

Figure 1 shows the schematic of the plasmonic metasurface lens. It consists of nanorods with spatially varying orientation in three different regions marked by I, II, and III, as shown in Figure 1a. The radius of region I (R-I) is r_1, and the inner radius and outer radius of region II (R-II) are r_1 and r_2. r_2 and r_3 are the inner radius and outer radius of region III (R-III). The relationship among r_1, r_2, and r_3 is governed by

$$r_1 : r_2 : r_3 = 1 : \sqrt{2} : \sqrt{3} \tag{1}$$

where r_1 = 40.0 μm, r_2 = 56.6 μm, and r_3 = 69.3 μm, which can ensure that the three regions R-I, R-II, and R-III have the same area. Therefore, the three parts of the metasurface will receive the same light energy flux when illuminated by a well-collimated incident light beam.

Prof. X. Chen, Prof. S. Zhang
School of Physics and Astronomy
University of Birmingham
Birmingham B15 2TT, UK
E-mail: x.chen@hw.ac.uk; s.zhang@bham.ac.uk
Prof. X. Chen, Prof. M. Chen, D. Wen, F. Yue
SUPA, Institute of Photonics and Quantum Sciences
School of Engineering and Physical Sciences
Heriot-Watt University
Edinburgh EH14 4AS, UK
Prof. M. Chen
Guangxi Experiment Center of Information Science
Guilin University of Electronic Technology
Guilin 541004, China
M. Q. Mehmood, Prof. C.-W. Qiu
Department of Electrical and Computer Engineering
National University of Singapore
4 Engineering Drive 3, Singapore 117576, Singapore
E-mail: chengwei.qiu@nus.ed.sg

The copyright line was amended 17 June 2015 after initial publication.

DOI: 10.1002/adom.201500110

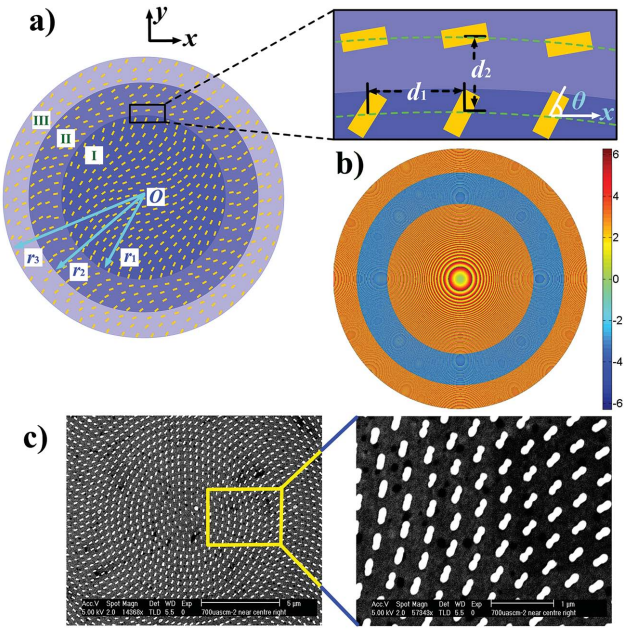

Figure 1. Schematic of a three-foci metasurface lens and SEM images of the fabricated plasmonic lens. a) Schematic illustration of the designed lens including three regions marked by I, II, and III. The radius of the region I (R-I) is r_1, the inner radius and the outer radius of the region II (R-II) are r_1 and r_2, and the inner radius and the outer radius of the region III (R-III) are r_2 and r_3. $r_1 = 40$ μm and $r_1 : r_2 : r_3 = 1 : \sqrt{2} : \sqrt{3}$. Each nanorod is 200 nm long, 50 nm wide, and 40 nm thick. All the nanorods are seated on the concentric circles. d_1 is the distance of two neighboring nanorods on the same concentric circle and d_2 is the difference of the radius of two neighboring concentric circles. b) Theoretical phase profile of the designed lens when illuminated by RCP light. The phase profile of the lens is achieved by adjusting the orientation angle φ of the individual nanorods. The phase shift in R-I and R-III ranges from 0 to 2π, but that in R-II ranges from -2π to 0. c) SEM images of the fabricated metasurface lens with lower and higher magnification.

In practice, it is very important that the phase change can be varied very smoothly from 0 to 2π. The phase distribution is realized by controlling the orientation angle φ of the gold nanorods relative to the x axis, as shown in Figure 1a. Each metallic nanorod is 200 nm long, 50 nm wide, and 40 nm thick. The center of all the nanorods is located on the concentric circles. d_1 is the distance between two neighboring nanorods on the same concentric circle and $d_1 = 400$ nm. d_2 is the difference of the radii of two neighboring concentric circles. The local phase change is simply governed by $\Phi = \pm 2\varphi$ and the sign is determined by the combination of the incidence/transmission polarizations. Specifically, in the above expression, "+" represents the sign of the phase shift for the incident beam with right circular polarization (RCP, denoted by $|R\rangle$) and the transmitted beam with left circular polarization (LCP, denoted by $|L\rangle$). Similarly, "–" represents the sign of that for the opposite incidence/transmission combination: LCP/RCP.

To focus an incident plane wave beam, the ultrathin flat lensing surfaces must have a spatially varying phase shift. In this way, the secondary waves emerging from the metasurface constructively interfere at the focal plane similar to the waves that emerge from conventional lenses. In order to achieve the phase profile equivalent to a conventional spherical lens, the relationship between the rotation angle φ and the center of each metallic nanorod r is governed by the following expression:

$$\varphi(r) = \pm k_0 (\sqrt{r^2 + f^2} - |f|) \tag{2}$$

where f is the focal length of the circular lens, $k_0 = 2\pi/\lambda$ is the free-space wave vector, and r represents the distance between the metallic nanorod and the center of the circular lens. Equation (2) shows that the sign of the required orientation angle depends on the helicity of the incident light beam. By considering Equation (2) and the relation $\Phi = \pm 2\varphi$, we can find an alternative to flipping the sign of the abrupt phase shift for the same incident circularly polarized light by flipping the sign of the orientation angle, which offers a new design methodology to develop multifoci metalens with different polarization states on the focal points. In our design, this relationship determined by Equation (2) can be rewritten in more detail as following:

$$\varphi(r) = \begin{cases} \pm k_0 (\sqrt{r^2 + f_1^2} - |f_1|) & 0 \le r \le r_1 \\ \mp k_0 (\sqrt{r^2 + f_2^2} - |f_2|) & r_1 < r \le r_2 \\ \pm k_0 (\sqrt{r^2 + f_3^2} - |f_3|) & r_2 < r \le r_3 \end{cases} \tag{3}$$

The above metalens with three longitudinal focal points can be considered as three sublenses with same axis and different focal lengths f_1, f_2, and f_3. The R-I ($0 \le r \le r_1$) of the metasurface contributes to the first sublens with a focal length f_1, while the R-II ($r_1 < r \le r_2$) and R-III ($r_2 < r \le r_3$) contribute to the other two sublenses with focal length f_2 and f_3, respectively. The designed values for f_1, f_2, and f_3 are, respectively, 60, 120, and 180 μm. Figure 1b shows the phase distribution of the metasurface lens as depicted by the Equation (3). For the same incident light (RCP), the sign of the phase shift generated by the metasurface in region R-I and R-III is positive, while that generated by the metasurface in region R-II is negative. This design can ensure that the polarity of the two neighboring sublenses is always opposite. For example, there will be two real focal points in the locations of the first and the third focal planes for a RCP incident light, while one virtual focal point will appear in the location of the second focal plane for the same incident light. When the helicity of the incident light is changed to LCP, all the polarities in the three sublenses will be switched.

A more detailed analysis of the multifoci metalens consisting of nanorods with spatially varying orientation is shown in **Figure 2**. Since a linearly polarized (LP, denoted by $|LP\rangle$) light beam can be decomposed into LCP and RCP components with the same amplitudes, there are three focal points in the real focal planes and three focal points in the virtual focal planes when the ultrathin flat metasurface lens is normally illuminated by the LP light. The three focal points will appear in the real focal planes and are denoted by F1, F2, and F3, respectively. The first and the third real focal points correspond to the RCP incident light, while the second real focal point corresponds to the LCP incident light. However, the polarization states in the above three focal points are LCP, RCP, and LCP respectively, as shown in Figure 2a. To analyze the focusing process when the (LP) light passes through the metasurface, the light intensity distribution along the longitudinal direction in the

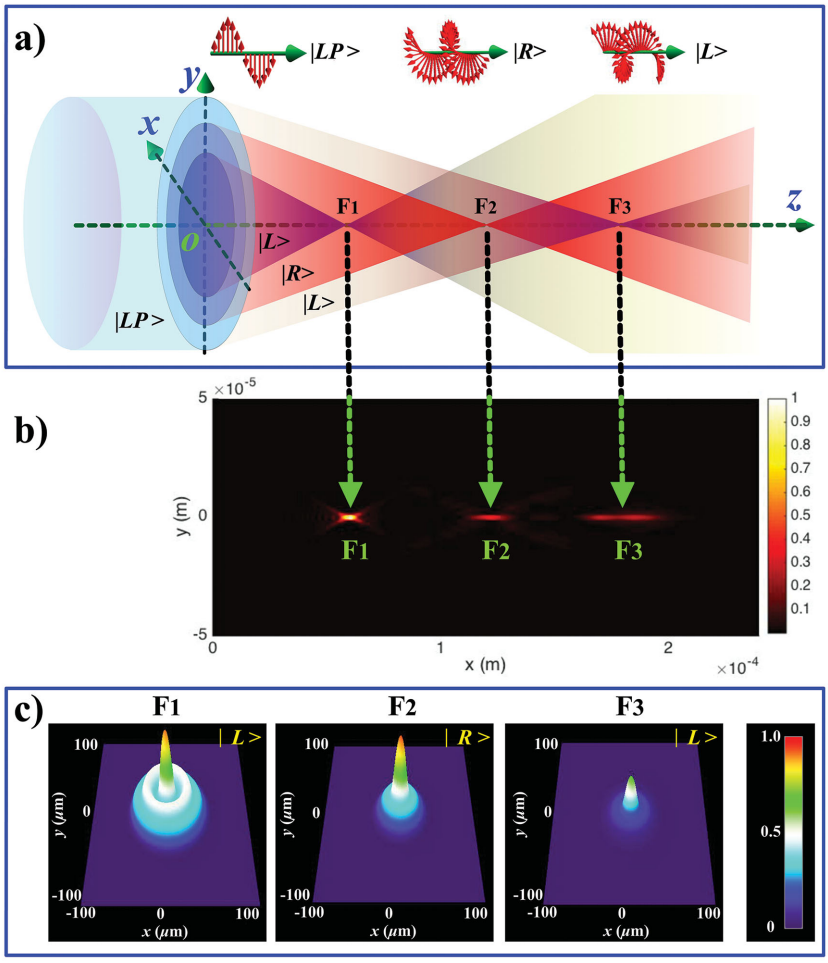

Figure 2. Illustration and simulation results of the metasurface lens. a) Schematic of the focusing performance of the metasurface lens when illuminated by a well-collimated linearly polarized light at normal incidence. Three focal planes are marked by F_1, F_2, and F_3, respectively. Three virtual focal points also exist in the virtual focal planes since the incidence of LP light means that LCP and RCP are available simultaneously. This figure only shows three real focal points. The symbols used for different polarization states are: |*LP*> for linear polarization, |*R*> for right circular polarization, and |*L*> left circular polarization. b) Theoretical intensity profile of the light behind the metalens in the *y*–*z* plane. c) Theoretical intensity distributions in the three focal planes at a wavelength of 740 nm. The maximal intensity decreases with the focal length, which is due to the increase of the focal depth.

meridional plane is given in Figure 2b. It is not surprising that three bright spots corresponding to the three real foci F_1, F_2, and F_3 are observed. Interestingly, the depth of focus (DOF) varies with the location of the focal points. DOFs are 3.50, 12.41, and 28.56 μm for F_1, F_2, and F_3, respectively. Theoretical intensity distributions at the focal planes of the three real foci at a wavelength of 740 nm are shown in Figure 2c. The maximal value of the intensity in the focal planes decreases with the increase of the focal length, which is due to the fact that the focus depth increases with the focal length, as shown in Figure 2b. Apart from the bright spots in the first and second focal planes, bright ring of light on the periphery also exists, which comes from the other two regions of the metasurface lens. Lenses with long focal depth are very important in optical coupling, optical imaging, and optical interconnections due to their large focusing range.[44,45] Three virtual focal points also exist on the object space since the incidence LP light can be decomposed into LCP and RCP which enable each sublens to work both as a converging lens and as a divergent lens.

The schematic of the optical measurement system is shown in **Figure 3**. To experimentally characterize the performance of the fabricated metalens, a tunable laser source (Fianium-SC400-PP) is used to generate the light beam with a wavelength of 740 or 670 nm. The circularly polarized light is generated by a QWP and a polarizer in front of the sample. The sample is mounted on a 2D translational stage. The light scattered by the metasurface with opposite circular polarization is collected by a 10×/0.30 objective and isolated with another pair of QWP and polarizer. The position of the objective is controlled by manually controlling the 3D translation stage.

To confirm the proposed approach, the fabricated longitudinal multifoci lens is experimentally investigated. First we evaluate the focusing performance of the metalens when illuminated with the linearly polarized light. **Figure 4** shows the experimentally measured intensity distributions in the six focal planes marked by I–VI at the location of –180, –120, –60, 60, 120, and 180 μm, respectively. The plane I, plane II, and plane III are the virtual focal planes on the object side and the plane IV, plane V, and plane VI are the real focal planes on the opposite side. Three virtual focal points and three real focal points are observed, which agrees very well with the theoretical prediction. The full width at half maximum (FWHM) is a parameter commonly used to describe the spot size of a focal point. The simulated FWHMs for the three real focal points in Figure 2c are 5.52, 5.95, and 6.82 μm, respectively. However, the experimentally measured FWHMs are 9.65, 10.37, and 11.52 μm, respectively. This deviation is due to the fabrication error and measurement accuracy.

To validate the polarity-switchable capability of such a lens, the sample is illuminated with a pure circularly polarized light beam. During the measurement process, the polarization direction of the two polarizers and the fast axes of the two quarter wave plates are parallel to each other, which can ensure that only the circularly polarized light with opposite helicity is detected. Figure 4 also shows the measured light intensity distributions in the six focal planes for two different incident/transmission polarization combinations: LCP/RCP (Figure 4b) and RCP/LCP (Figure 4c). As shown by Figure 4b for the LCP incident beam, we observe two bright spots in the virtual focal planes and one in the real focal plane. Compared with the corresponding figures in Figure 4a, three focal points are missing

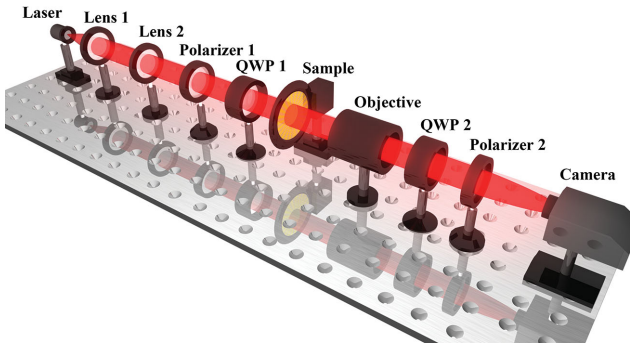

Figure 3. Experimental setup for measuring the transmitted light intensity distribution. The experimental system includes the supercontinuum laser source, several lenses, two polarizers, two quarter waveplates (QWP), two translation stages, an objective, and a CCD camera. The sample is mounted on the 2D translation stage and the objective is mounted on the 3D translation stage. The transmission after the sample is collected by collected by a 10×/0.30 objective and coupled into the CCD camera.

since the incident light is pure LCP. When the polarizations of the incident and transmitted beam are switched to RCP and LCP respectively, the focusing behavior for the same lens is reversed, as shown in Figure 4c. One bright spot appears in the virtual focal plane and two in the real focal planes, which lie on the locations of the missing light spots in Figure 4b. The conversion in the focusing properties from positive (negative) to negative (positive) is solely attributed to the helicity change of the circular polarization for the incident light, which agrees perfectly with the theoretical prediction. We also notice that the ratio of signal-to-noise in Figure 4b,c is much better than that in Figure 4a, which is due to the fact that the light that does not contribute to focusing cannot be filtered out in the experiment in Figure 4a.

The polarization conversion of the metasurface lens is based on Pancharatnam–Berry phase,[48,49] which is not affected by the incident wavelength and can enable the metasurface lens to work in the broadband. However, the wavelength of the incident light plays an important part in conversion efficiency, which can reach the maximum value only when the incident light resonates with the metallic nanorods. The conversion efficiency of the anomalously refracted light can be greatly enhanced by using a dielectric metasurface, which will decrease the ohmic losses and improve the scattering cross sections of the metal nanorods.[39,50] High efficiency and broadband property of the proposed device can also be achieved by using reflective-type metasurface.[51] The developed longitudinal multifoci metalenses are very interesting since they can be used to simultaneously trap particles at different longitudinal positions and rotate them with different directions (clockwise or anticlockwise), which might find application in biology, physical chemistry, and biomedicine. The longitudinal position and the number of the focal points can be engineered at will. Theoretically, the number of focal points can be

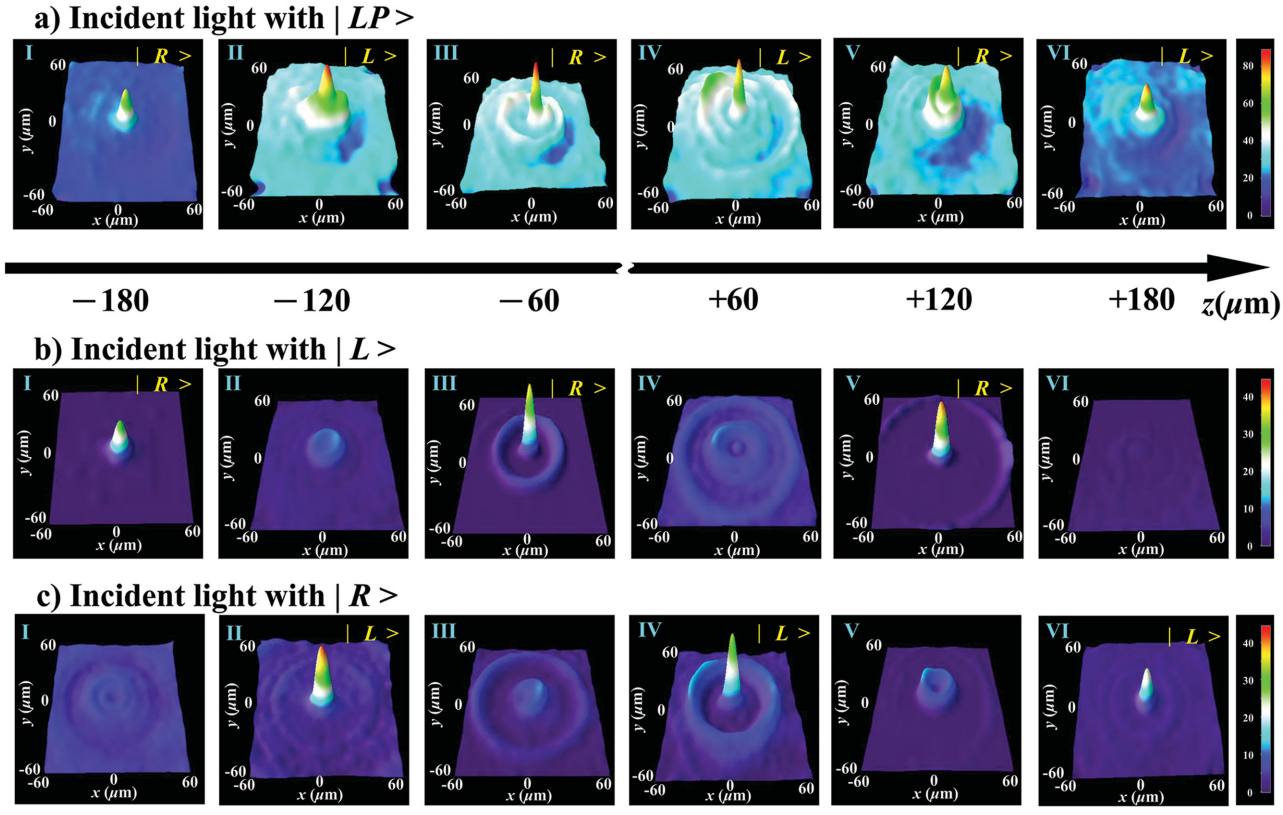

Figure 4. Experimentally measured light intensity distributions in the six focal planes at the wavelength of 740 nm. The sample is illuminated by a parallel light beam with a) linear polarization (|*LP*>), b) left circular polarization (|*L*>), and c) right circular polarization (|*R*>). The three virtual focal planes are located at −180, −120, and −60 μm, respectively, while the three real focal planes are located at +60, +120, and +180 μm, respectively.

increased by increasing the number of regions with different radii. However, the metallic nanorods in a given region not only contribute to one specific focal point but also add background noise to other focal points. Consequently, the quality of each focal point will become worse with an increase in the number of focal points. Furthermore, the polarity of each focal point is switchable, depending on the helicity of the circular polarization. The control of light focal points and the helicity is of great importance in optical tweezers, offering a wide range of applications including the study of cells and molecules, cancer treatment and DNA exploration.[52–54] In addition, the orbital angular momentum of light, related to the generator of rotations in quantum mechanics, has been typically associated with its circular polarization components. This orbital angular momentum content is not just a formal property, but a very concrete one that can have significant mechanical effects, which can be directly used in quantum information processing.[55–57]

We have experimentally demonstrated a longitudinal multi-foci flat metasurface lens with a thickness of 40 nm. The measured intensity distribution of each focal point agrees with very well with the theoretical prediction. The longitudinal position and the number of the focal points can be tailored to meet the specific requirement, which may find application in particle manipulation, imaging, and quantum information processing. The ultrathin multifunction metasurface lenses are of great interest since flat lenses based on metasurfaces are compatible with standard semiconductor fabrication process. These types of exciting new ultrathin lenses open a new avenue to achieve a high density of functionality, effectively scaling down the size of photonic systems.

Experimental Section

To fabricate the designed nanoantenna structures, the standard electron-beam lithography (EBL) and lift-off process are used. A positive polymethyl methacrylate (PMMA) resist film is spin coated on an indium-tin-oxide coated glass substrate and then baked at 180 °C for 2 min. The nanostructures are defined on the PMMA film by EBL and a 40 nm gold film is deposited on the sample via thermal evaporator. Finally, the plasmonic metalens is achieved by a subsequent lift-off procedure. A circularly polarized laser beam is generated by a QWP and a polarizer in front of the sample. The light scattered by the metasurface is collected by a 10×/0.30 infinity corrected objective and isolated with another pair of QWP and polarizer. All the optical components and the charge-coupled device (CCD) camera are positioned in a straight line. By controlling the position of the objective, a CCD camera is used to image different focal planes at different positions.

Acknowledgements

X.C. acknowledges the Engineering and Physical Sciences Research Council of the United Kingdom (Grant Ref: EP/M003175/1) and Renishaw-Heriot Watt Strategic Alliance. M. Chen acknowledges the support from the Chinese Scholarship Council (CSC, No. 201208455034).

Received: February 20, 2015
Revised: April 9, 2015
Published online: May 12, 2015

[1] P. Deymier, *Acoustic Metamaterials and Photonic Crystals*, Springer-Verlag, Berlin **2013**.
[2] Y. B. Xie, W. Q. Wang, H. Y. Chen, A. Konneker, B. I. Popa, S. A. Cummer. *Nat. Commun.* **2014**, *5*, 5553.
[3] A. Colombi, P. Roux, M. Rupin, *J. Acoust. Soc. Am.* **2014**, *136*, EL192.
[4] M. Kadic, T. Bückmann, R. Schittny, M. Wegener, *Rep. Prog. Phys.* **2013**, *76*, 126501.
[5] T. A. Schaedler, A. J. Jacobsen, A. Torrents, A. E. Sorensen, J. Lian, J. R. Greer, L. Valdevit, W. B. Carter, *Science* **2011**, *334*, 962.
[6] B. Florijn, C. van Hecke, M. Coulais, *Phys. Rev. Lett.* **2014**, *113*, 175503.
[7] X. Zheng, H. Lee, T. H. Weisgraber, M. Shusteff, J. DeOtte, E. B. Duoss, J. D. Kuntz, M. M. Biener, Q. Ge, J. A. Jacson, S. O. Kucheyev, N. X. Fang, C. M. Spadaccini, *Science* **2014**, *344*, 1373.
[8] S. Zhang, D. A. Genov, C. Sun, X. Zhang, *Phys. Rev. Lett.* **2008**, *100*, 123002.
[9] N. Engheta, R. W. Ziolkowski, *Metamaterials: Physics and Engineering Explorations*, IEEE-Wiley, New York **2006**.
[10] C. Caloz, T. Itoh, *Electromagnetic Metamaterials: Transmission Line Theory and Microwave Applications*; IEEE-Wiley, New York, **2006**.
[11] W. S. Cai, V. Shalaev, *Optical Metamaterials: Fundamentals and Applications*, Springer, New York **2010**.
[12] D. H. Werner, D. H. Kwon, *Transformation Electromagnetics and Metamaterials: Fundamental Principles and Applications*, Springer-Verlag, London **2014**.
[13] J. B. Pendry, D. Schurig, D. R. Smith, *Science* **2006**, *312*, 1780.
[14] F. Capolino, *Theory and Phenomena of Metamaterials*, CRC Press, New York **2009**.
[15] N. Fang, H. Lee, C. Sun, X. Zhang, *Science* **2005**, *308*, 534.
[16] H. Lee, Z. W. Liu, Y. Xiong, C. Sun, X. Zhang, *Opt. Express* **2007**, *15*, 15886.
[17] U. Leonhardt, *Nature* **2011**, *471*, 292.
[18] V. M. Shalaev, *Science* **2008**, *322*, 384.
[19] D. Schurig, J. B. Pentry, D. R. Smith, *Opt. Express* **2006**, *14*, 9794.
[20] U. Leonhardt, T. G. Philbin, *Geometry and Light: The Science of Invisibility*, Dover Publications, Inc., Mineola, NY, **2010**.
[21] B. L. Zhang, *Light: Sci. Appl.* **2012**, *1*, e32.
[22] N. F. Yu, P. Genevet, M. A. Kats, F. Aieta, J. P. Tetienne, F. Capasso, Z. Gaburro, *Science* **2011**, *334*, 333.
[23] N. F. Yu, F. Capasso, *Nat. Mater.* **2014**, *13*, 139.
[24] F. Aieta, P. Genevet, N. F. Yu, M. Kats, Z. Gaburro, F. Capasso, *Nano Lett.* **2012**, *12*, 1702.
[25] P. Genevet, N. F. Yu, F. Aieta, J. Lin, M. A. Kats, R. Blanchard, M. O. Scully, Z. Caburro, F. Capasso, *Appl. Phys. Lett.* **2012**, *100*, 013101.
[26] G. D'Aguanno, N. Mattiucci, M. Bloemer, A. Desyatnikov, *Phys. Rev. A* **2008**, *77*, 043825.
[27] X. Chen, L. L. Huang, H. Mühlenbernd, G. X. Li, B. F. Bai, Q. F. Tan, G. F. Jin, C. W. Qiu, S. Zhang, T. Zentgraf, *Nat. Common.* **2012**, *3*, 1198.
[28] X. Chen, L. Huang, H. Mühlenbernd, G. Li, B. Bai, Q. Tan, G. Jin, C.-W. Qiu, T. Zentgraf, S. Zhang, *Adv. Opt. Mater.* **2013**, *1*, 517.
[29] N. F. Yu, F. Aieta, P. Genevet, M. A. Kats, Z. Gaburro, F. Capasso, *Nano Lett.* **2012**, *12*, 6328.
[30] X. B. Yin, Z. L. Ye, J. Rho, Y. Wang, X. Zhang, *Science* **2013**, *339*, 1405.
[31] N. Shitrit, I. Yulevich, E. Maguid, D. Ozeri, D. Veksler, V. Kleiner, E. Hasman, *Science* **2013**, *340*, 724.
[32] L. L. Huang, X. Z. Chen, B. F. Bai, Q. F. Tan, G. F. Jin, T. Zentgraf, S. Zhang, *Light: Sci. Appl.* **2013**, *2*, e70.
[33] J. Lin, J. P. Balthasar Mueller, Q. Wang, G. H. Yuan, N. Antoniou, X. C. Yuan, F. Capasso, *Science* **2013**, *340*, 331.

[34] A. Pors, M. G. Nielsen, T. Bernardin, J. C. Weeber, S. I. Bozhevolnyi, *Light: Sci. Appl.* **2014**, *3*, e197.
[35] S. Larouche, Y. J. Tsai, T. Tyler, N. M. Jokerst, D. R. Smith, *Nat. Mater.* **2012**, *11*, 450.
[36] L. L. Huang, X. Z. Chen, H. Mühlenbernd, H. Zhang, S. M. Chen, B. F. Bai, Q. F. Tan, G. F. Jin, K. W. Cheah, C. W. Qiu, J. S. Li, T. Zentgraf, S. Zhang, *Nat. Commun.* **2013**, *4*, 3808.
[37] C. M. Chang, M. L. Tseng, B. H. Cheng, C. H. Chu, Y. Z. Ho, H. W. Huang, Y. C. Lan, D. W. Huang, A. Q. Liu, D. P. Tsai, *Adv. Mater.* **2013**, *25*, 1118.
[38] F. Zhou, Y. Liu, W. Cai, *Opt. Express* **2013**, *21*, 4348.
[39] D. M. Lin, P. Y. Fan, E. Hasman, M. L. Brongersma, *Science* **2014**, *345*, 298.
[40] P. R. West, J. L. Stewart, A. V. Kildishev, V. M. Shalaev, V. V. Shkunov, F. Strohkendl, Y. A. Zakharenkov, R. K. Dodds, R. Byren, *Opt. Express* **2014**, *22*, 26212.
[41] P. J. Valle, M. P. Gagigal, *Opt. Lett.* **2012**, *37*, 1121.
[42] P. Gracia, G. Dorronsoro, S. Marcos, *Opt. Lett.* **2013**, *38*, 3526.
[43] V. F. Canales, P. Valle, J. E. Oti, M. P. Gagigal, *Opt. Commun.* **2006**, *257*, 247.
[44] J. Jia, C. Zhou, L. Liu, *Opt. Commun.* **2003**, *228*, 271.
[45] M. Kang, T. H. Feng, H. T. Wang, J. S. Li, *Opt. Express* **2012**, *14*, 15882.
[46] X. Y. Jiang, J. S. Ye, J. W. He, X. K. Wang, D. Hu, S. F. Feng, Q. Kan, Y. Zhang, *Opt. Express* **2013**, *21*, 30030.
[47] T. Tanemura, K. C. Balram, D. S. Ly-Gagnon, P. Wahl, J. S. White, M. L. Brongersma, D. A. B. Miller, *Nano Lett.* **2011**, *11*, 2693.
[48] S. Pancharatnam, *Proc. Indian Acad. Sci. A* **1956**, *44*, 247.
[49] M. V. Berry, *J. Mod. Opt.* **1987**, *34*, 1401.
[50] A. Arbabi, Y. Horie, M. Bagheri, A. Faraon, arXiv:1411.1494v1, **2014**.
[51] G. Zheng, H. Mühlenbernd, M. Kenney, G. Li, T. Zentgraf, S. Zhang, *Nat. Nano* **2015**, *10*, 308.
[52] Y. Choe, J. W. Kim, K. K. Shung, E. S. Kim, in Joint Conference of the IEEE International, DOI: 10.1109/FCS.2011.5977900.
[53] O. V. Angesky, A. Y. Bekshaev, P. P. Masksimyak, A. P. Maksimyak, I. I. Mokun, S. G. Hanson, C. Y. Zenkova, A. V. Tyurin, *Opt. Express* **2012**, *20*, 11351.
[54] S. Bayoudh, T. A. Nieminen, N. R. Heckenberg, H. Rubinsztein-Dunlop, *J. Mod. Opt.* **2003**, *50*, 1581.
[55] Y. M. Li, J. Kim, M. J. Escuti, *Appl. Opt.* **2012**, *51*, 8236.
[56] J. Leach, M. J. Padgett, S. M. Barnett, S. Franke-Arnold, J. Courtial, *Phys. Rev. Lett.* **2002**, *88*, 257901.
[57] P. Torres, L. Torner, *Twisted Photons: Applications of Light with Orbital Angular Momentum*, Wiley-VCH, Weinheim, Germany **2011**.

